

## ABC-SN: Attention Based Classifier for Supernova Spectra

WILLOW FOX FORTINO,<sup>1</sup> FEDERICA B. BIANCO,<sup>1,2,3,4</sup> PAVLOS PROTOPAPAS,<sup>5</sup> DANIEL MUTHUKRISHNA,<sup>6</sup> AND  
AUSTIN BROCKMEIER<sup>3,7,8</sup>

<sup>1</sup>*Department of Physics and Astronomy, University of Delaware, Newark, DE 19716, USA*

<sup>2</sup>*Joseph R. Biden, Jr. School of Public Policy and Administration, University of Delaware, Newark, DE 19716, USA*

<sup>3</sup>*Data Science Institute, University of Delaware, Newark, DE 19716, USA*

<sup>4</sup>*Vera C. Rubin Observatory, Tucson, AZ, USA*

<sup>5</sup>*John A. Paulson School of Engineering and Applied Sciences, Harvard University, Cambridge, MA, 02138, USA*

<sup>6</sup>*Kavli Institute for Astrophysics and Space Research, Massachusetts Institute of Technology, Cambridge, MA 02139, USA*

<sup>7</sup>*Department of Electrical and Computer Engineering, University of Delaware, Newark, DE, USA*

<sup>8</sup>*Department of Computer and Information Sciences, University of Delaware, Newark, DE, USA*

### ABSTRACT

While significant advances have been made in photometric classification ahead of the millions of transient events and hundreds of supernovae (SNe) each night that the Vera C. Rubin Observatory Legacy Survey of Space and Time (*LSST*) will discover, classifying SNe spectroscopically remains the best way to determine most subtypes of SNe. Traditional spectrum classification tools use template matching techniques (Blondin & Tonry 2007) and require significant human supervision. Two deep learning spectral classifiers, DASH (Muthukrishna et al. 2019) and SNIascore (Fremling et al. 2021) define the state of the art, but SNIascore is a binary classifier devoted to maximizing the purity of the SN Ia-norm sample, while DASH is no longer maintained and the original work suffers from contamination of multi-epoch spectra in the training and test sets. We have explored several neural network architectures in order to create a new automated method for classifying SN subtypes, settling on an attention-based model we call ABC-SN. We benchmark our results against an updated version of DASH, thus providing the community with an up-to-date general purpose SN classifier. Our dataset includes ten different SN subtypes including subtypes of SN Ia, core collapse and interacting SNe. We find that ABC-SN outperforms DASH, and we discuss the possibility that modern SN spectra datasets contain label noise which limit the performance of all classifiers.

### 1. INTRODUCTION

As the field of astronomy stands on the brink of a data revolution brought about by the Vera C. Rubin Observatory’s Legacy Survey of Space and Time (*LSST*), the astronomy community braces for an influx of data at an unprecedented scale. The *LSST* will observe millions of transient events nightly, with supernovae (SNe) poised to form a substantial fraction. This will stretch the existing spectral follow-up infrastructure to its limits, necessitating a paradigm shift in our approach to handling the flood of SN candidates that will emerge from the *LSST* alert stream. Effective classification of SN subtypes is crucial for our understanding of stellar

evolution and the distribution of elements in the universe.

Minkowski (1941) introduced the first SN classification scheme by dividing the SNe that did not contain hydrogen (Type I) from those that did (Type II). In his review, Filippenko (1997) describes the evolved classification scheme as of the late 1990s, with further subclasses of SNe based on the early-epoch chemical composition identified in the spectra. While all Type I lack the presence of hydrogen (H) lines, Type Ia spectra display intense Si<sup>1</sup> lines, Type Ib spectra exhibit pronounced HeI lines, and Type Ic spectra show neither.

SNe Ib, Ic, and II are core-collapse SNe (Janka et al. 2012; Modjaz et al. 2019) with progenitor stars of mass of  $> 8M_{\odot}$  (Woosley & Weaver 1986; Woosley & Janka

Corresponding author: Willow Fox Fortino  
fortino@udel.edu

<sup>1</sup> Singly-ionized Si.

2005; Couch 2017). On the other hand, SNe Ia are the result of thermonuclear explosions (Röpke 2007) produced when a white dwarf (WD) star is accreting matter from a nearby star (Mazzali et al. 2007) beyond the “Chandrasekhar limit” of  $\sim 1.4M_{\odot}$  (although in practice both sub- and super-Chandrasekhar progenitors have been identified, Andrew Howell et al. *e.g.*, 2006; Hicken et al. *e.g.*, 2007, see for example Woosley & Kasen 2011 for a theoretical approach). Carbon fusion occurs quickly and explosively, producing the SNe that are observed. The intrinsic brightness of SNe Ia can be calculated from their temporal evolution and color, and they are therefore known as “standard(izable) candles” and cosmologists use SNe Ia to study dark energy and the expansion of the Universe (Riess et al. 1998; Perlmutter et al. 1999).

Yet, further ‘subtypes’ of the mentioned SN types exist that are also distinguished by their spectral lines. Some progenitors are surrounded by circumstellar material (csm), which interacts with their SNe, causing differences in spectra and leading to their own classification (*e.g.*, SN IIn and Ibn). Some SNe are identified as abnormal and receive their own classification. Particularly important for cosmology is the identification of specific SN Ia subtypes (*e.g.*, SN Ia 91T, 91bg) whose properties may deviate from the canonically formalized standardization that enables measures of the Hubble constant (*e.g.*, Sasdelli et al. 2016; Blondin et al. 2012). In some cases, photometric properties also modify a classification, as in the case of SN IIP, showing a plateau in the light curve and SN IIL, showing a linear decrease, while, ostensibly, they may present the same spectroscopically (Gal-Yam 2017, but also see Kou et al. 2020, conversely, note that spectroscopically unusual SNe may present within the normal range photometrically Khakpash et al. 2024).

Additional explosion methods (*e.g.*, pair instability Woosley 2017; Kasen et al. 2011), and several more types and subtypes of Super-Luminous Supernovae exist, but are not addressed in this work; see Moriya et al. (2018) for a review.

Altogether, this brief introduction only scratches the surface of a complex, and, apparently, ever-growing taxonomy. Typing SN reflects sometimes completely different progenitor or explosion mechanisms, sometimes nuanced differences in a continuum of parameters such as how much material was stripped before the explosion, mass, metallicity of the progenitor environment, etc. The reader should keep this in mind and throughout this report we discuss how this may impact the result of automated classifiers.

While photometric classification methods (*e.g.*, Boone 2019; Möller & de Boissière 2020; Qu et al. 2021; Shah et al. 2025) have made significant advances motivated by the upcoming *LSST* which will discover too many and too faint SNe for comprehensive spectroscopic classification, and multimodal models are starting to appear (Zhang et al. 2024), classifying SNe spectroscopically remains the most common way to determine most subtypes of SNe.

Currently, the most prevalent method for the classification of SN subtypes is Supernova Identification (Blondin & Tonry 2007, SNID), which performs a cross-correlation with an extensive library of labeled SNe and template spectra. Though this approach has been a mainstay in the field due to its reliability and interpretability, the oncoming data deluge from the *LSST* presents a scalability challenge that SNID may struggle to meet efficiently. As SN science evolves, template matching methods require continuous, careful reclassification. Meanwhile, machine learning models like *SNiascore* (Fremling et al. 2021), which have shown proficiency in classifying Type Ia SNe with the low-resolution spectral data from the *SEDMachine* (Blagorodnova et al. 2018, *SEDM*), have yet to demonstrate the same adaptability for a wider variety of SN subtypes.

This paper introduces ABC-SN the ‘Attention-Based Classifier for Supernovae’, a novel approach to SN classification that leverages the multi-head attention layer in the transformer neural network architecture (Vaswani et al. 2017), a model that has significantly impacted the field of natural language processing and was subsequently adapted for innumerable applications from computer vision (Dosovitskiy et al. 2020) to time series forecasting (Zhou et al. 2021). Like the complex web of syntax and semantics in human languages, SN spectra contain intricate patterns — spectral features — that signal the presence of specific elements, stellar structure patterns, and determine a SN’s subtype. We posit that the transformer’s ability to parse these complex patterns in language could be directly applicable to spectral classification. Applications of transformer-derived architectures to spectroscopy outside of astrophysics include (Cai et al. 2022) and a number of models for application on hyperspectral imaging (*e.g.*, He et al. 2021). In astrophysics, see for example Zhang et al. (2024) and Koblishke & Bovy (2024).

An important precursor to our work is the Deep Automated Supernova and Host (DASH) classifier (Muthukrishna et al. 2019). DASH is a convolutional neural network designed to determine subtype, age, redshift, and host galaxy from SN spectra. Compared to subtype

classification, DASH tackles a significantly more complex task. Because DASH is the only other general-purpose, machine learning based, spectral SN classifier, we will compare ABC-SN to DASH’s performance as a subtype classifier by aggregating over its age classification.

The goal of this research is to introduce a classifier that surpasses the limitations of SNID, SNiascore, and DASH. To that end, we have assembled a dataset of high-resolution SN spectra to train this new attention-based classifier on. The full composition, provenance, and pre-processing of the data are discussed in Section 3. The details of how ABC-SN is trained and evaluated is discussed in Section 4.

## 2. RETRAINING DASH

To establish a benchmark for the automated classification of SN spectra, we retrain DASH with four goals in mind: To replicate DASH’s published results; To determine DASH’s results when compensating for overfitting; To determine DASH’s results without dataset contamination; To provide a benchmark to compare ABC-SN to. To that end, we retrained DASH in three different ways, the results of which are shown in Figure 1.

In order to compare ABC-SN to DASH, we must consider DASH’s training scheme. Using code from Muthukrishna et al. (2019), we set the training set fraction to 50% and find that the initial  $\sim 2000$  spectra in both the training and test sets are magnified to  $\sim 130,000$  spectra in each set after data augmentation.

The batch size during DASH training is 50, which means that it takes  $\sim 2600$  batch iterations to complete one training epoch. For this reason, we propose the concept of a ‘pseudo-epoch’. One pseudo-epoch is equivalent to the number of DASH batches it takes such that  $50 \times N_{\text{batches}} = N_{\text{train}}$  where  $N_{\text{train}}$  is the size of the training set *before* data augmentation. The pseudo-epoch helps us compare training times and overfitting between DASH and ABC-SN and does not affect the way that DASH is retrained.

A dataset of SN spectra poses a unique complication: the same SN may be observed multiple times at different epochs in the lifetime of the transient. For instance, our dataset is comprised of 3,764 spectra from 498 objects, where 144 SNe contribute 10 or more spectra each. While SNe do evolve, key signatures of the cosmic explosion will persist over time. Thus, all spectra from the same SN are highly correlated; they are typically more self-similar than similar to spectra of other SNe of the same subtype.

All spectra from one SN must go into either the training or the test set. Contamination of spectra from the same object in the training and test set, even if taken

at different epochs, would artificially inflate the performance of the model once results were calculated on the test set.

However, since DASH was designed to identify the epoch at which a spectrum was collected (in addition to the SN type), this exact type of contamination affected DASH.

We retrain DASH in three steps (see Figure 1). We first run DASH in a way that mimics the original published results: the contamination in the training and test sets is present, and the model is trained for 500,000 batches. This satisfies our first goal (Figure 1, left).

Then we curtail overfitting by implementing an early stopping protocol which halts training if model performance doesn’t increase. Specifically, if test set F1-score does not increase by 0.005 for 10 pseudo-epochs, we stop training. Also, if training set F1-score exceeds the test set by 0.10 for 10 pseudo-epochs, we halt training. This satisfies our second goal (Figure 1, middle).

In the third and final run, we correct the dataset contamination while also implementing the early stopping protocol. This satisfies our third goal.

All three instances of DASH are trained with all original 16 SN subtypes. However, in Figure 1 we present confusion matrices for these models including only the ten subtypes seen in Figure 2. We also note that we retrain DASH on a low-resolution ( $R = \frac{\lambda}{\Delta\lambda} = 100$ ) spectral dataset (see Section 3.2 for justification). These two changes satisfy our fourth goal and thus provide a new performance benchmark for the automated classification of SN spectra with DASH (Figure 1, right). This benchmark F1-score is  $F1_{\text{DASH}} = 0.40$ .

Note that Fremling et al. (2021) also offers a comparison of SNiascore with DASH. However, they use low-resolution spectra from the SEDM and do not retrain DASH on low-resolution spectra. Thus, their performance comparison is not fair. We chose to retrain DASH on our dataset to offer a rigorous performance comparison.

## 3. DATA

A direct comparison with DASH was a goal from the outset, so we start with the same dataset used to train DASH: the spectral library that comprises the SNID templates. Furthermore, we start with the SNID labels as our ground truth. However, we make several updates and modifications to this dataset. The original spectra in our dataset were gathered from a variety of sources. In addition to the core SNID library, they contain a catalog of stripped envelope SNe (SESNe) that is included from Liu & Modjaz (2015); Modjaz et al. (2014, 2016); Liu et al. (2016) (which were integrated into the SNID library after DASH was trained). SESNe are SNe where

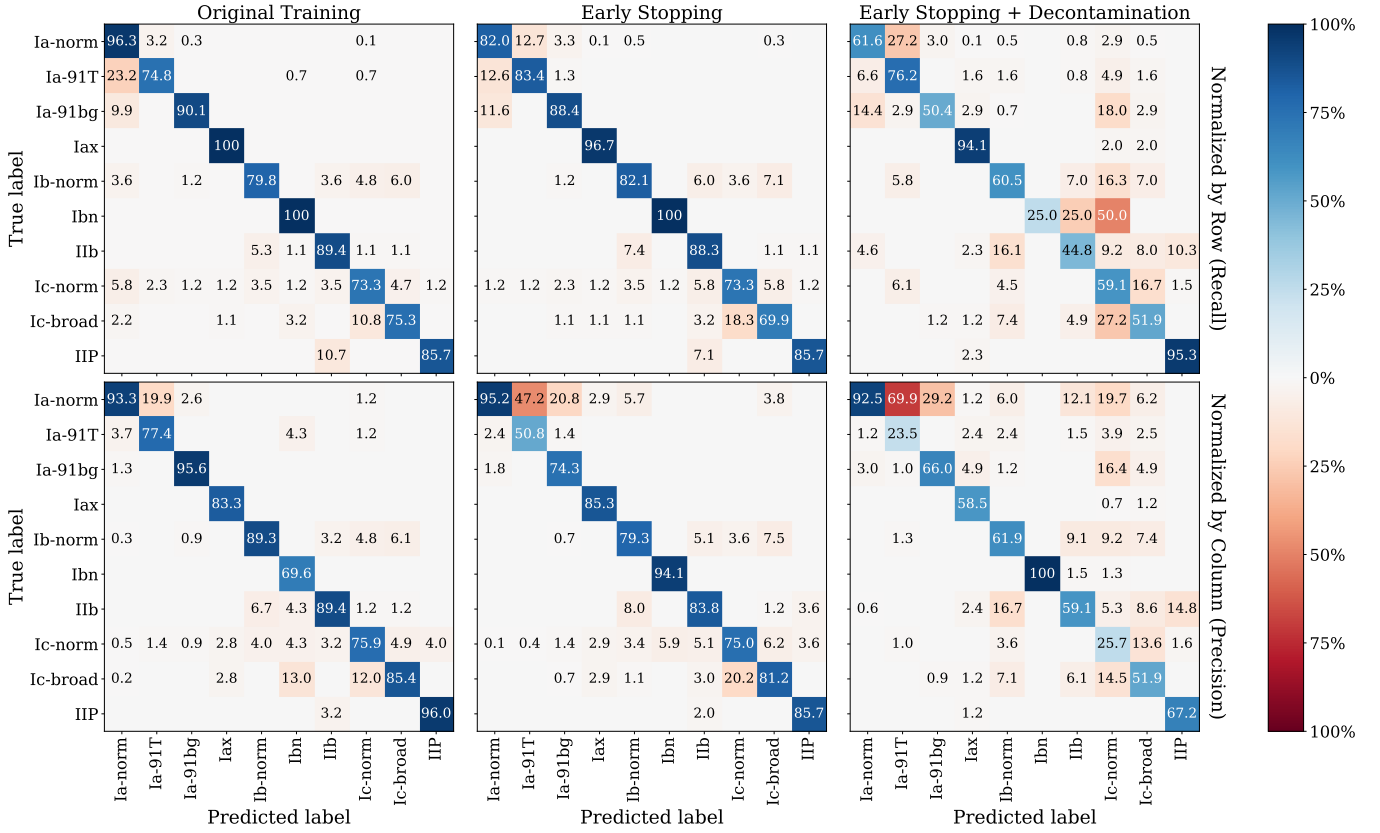


**Figure 1.** DASH SN classifier performance under different training schemas for the classes considered in this work (Section 3). The *top* row shows model completeness (*i.e.*, recall) by normalizing across true labels. The *bottom* row shows purity (*i.e.*, precision) by normalizing across the predictions. In each confusion matrix, cells on the diagonal (correct classifications) are plotted in shades of blue and off-diagonal (incorrect) in shades of red. In each cell, the percentage of objects labeled according to the row and predicted according to the column is reported. When no objects correspond to that label and prediction, the number (0%) is omitted. *Left:* DASH (Muthukrishna et al. 2019) retrained with the original training schema, which includes the same SN at different epochs in the training and test set and allows training to complete to 12,500 pseudo-epochs (see Section 2), inducing significant overfitting. While the confusion matrix looks best, the transferability and reliability of this model are in question due to severe overfitting. *Middle:* The same training and test sets are used, but training is stopped early to prevent overfitting (see Section 2). *Right:* The train-test split has been modified to ensure that all spectra from each SN appear *only* in either the training or the test set. We will compare ABC-SN to this final model. Note that DASH is retrained on  $R = 100$  spectra (see Section 3.2).

the progenitor star’s outer shell of hydrogen and helium have been removed prior to explosion and refer to the subtypes Ib-norm, IIb, Ic-norm and Ic-broad.

We also include a catalog of spectra from the Berkeley SN Ia Program (Silverman et al. 2012, *BSNIP*).

The SNID templates are described in Blondin & Tonry (2007); Blondin et al. (2012) and were originally collected from the *SUSPECT* public archive (Yaron & Gal-Yam 2012), the CfA Supernova Archive and the CfA Supernova Program (Matheson et al. 2008; Blondin et al. 2012) and were retrieved by Muthukrishna et al. (2019).

Our dataset is composed of 3,764 spectra from 498 SNe at a spectral resolution  $R \equiv 738$ . These spectra were selected because of their generally high signal-to-noise-ratio (SNR) and uniformity of preprocessing. The

dataset represents 17 SN subtypes, but there is only one SN II-pec in the dataset, sn1987A (Kunkel et al. 1987). Thus we removed this SN and its 241 associated spectra.

We have also removed six other SN subtypes from the dataset: Ia-csm, Ib-pec, Ic-pec, IIL, IIn, and Ia-pec. The first five were removed because we had fewer than 50 spectra total after preprocessing. Ia-pec SN spectra were removed because we hypothesized that the ‘peculiar’ SN subtypes were historically used as a catch-all ‘other’ classification that was harming our model’s performance.

After preprocessing, the number of spectra from each of the remaining ten SN subtypes is illustrated in Figure 2. Table 1 contains the number of each spectrum present in the dataset at each stage of our data prepa-

SN Subtype (SNe)	Before PP	After PP	Trn Set	Trn Set (w/ Aug)	Tst Set
Ia-norm (319)	2387 (53.5%)	2114 (56.2%)	1058 (56.2%)	1058 (9.6%)	1056 (56.2%)
Ia-91T (36)	398 (8.9%)	348 (9.2%)	163 (8.7%)	1141 (10.3%)	185 (9.8%)
Ia-91bg (42)	264 (5.9%)	232 (6.2%)	101 (5.4%)	1111 (10.1%)	131 (7.0%)
Iax (6)	68 (1.5%)	62 (1.6%)	28 (1.5%)	1064 (9.6%)	34 (1.8%)
Ib-norm (22)	270 (6.0%)	211 (5.6%)	99 (5.3%)	1089 (9.9%)	112 (6.0%)
Ibn (3)	31 (0.7%)	27 (0.7%)	9 (0.5%)	1062 (9.6%)	18 (1.0%)
IIf (19)	328 (7.3%)	232 (6.2%)	139 (7.4%)	1112 (10.1%)	93 (4.9%)
Ic-norm (21)	263 (5.9%)	206 (5.5%)	112 (5.9%)	1120 (10.2%)	94 (5.0%)
Ic-broad (24)	279 (6.2%)	228 (6.1%)	117 (6.2%)	1170 (10.6%)	111 (5.9%)
IIP (6)	176 (3.9%)	104 (2.8%)	58 (3.1%)	1102 (10.0%)	46 (2.4%)

**Table 1.** This table shows the exact distribution of the number of SN spectra across each of the ten SN subtypes. The number of SNe for each subtype is shown in parentheses next to the subtype name. The *first column* shows the distribution of the spectra we collected before any preprocessing. The *second column* contains the same information as in Figure 2 and shows the distribution after the preprocessing steps, which remove some known bad spectra. The *third* and *fifth columns* show the distributions of the training and test set split. The *fourth column* shows the final distribution of the training set after the data augmentation techniques (see Section 3.4) have been applied. Note how each class is represented approximately evenly in the training set after augmentation, while the test set preserves the original class imbalance.

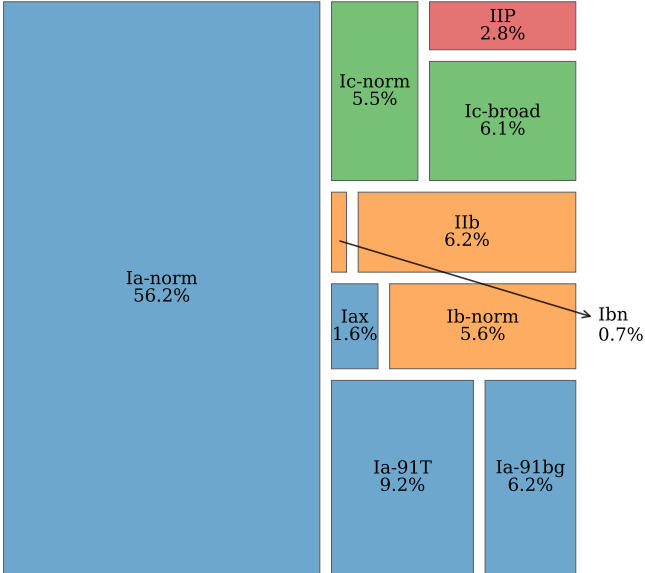


**Figure 2.** A treemap plot showing the composition of our dataset of SN spectra after preprocessing. The size of each rectangle corresponds to the proportion of the ten SN subtypes in our dataset. The color of each rectangle corresponds to which main SN type — Ia, Ib, Ic or II — the subtype belongs to. There are 3,764 total spectra from 498 SNe. This plot shows the extreme class imbalance in this dataset, with  $\sim 73\%$  of the spectra coming from SN Ia. This poses a profound challenge for machine learning. The content of this plot is equivalent to the content of the second column in Table 1.

ration. All data preparation stages are detailed in Section 3.1.

### 3.1. Pre-preprocessing

Any spectrum taken directly from a spectrograph is not yet suitable for training or classification. After processing the 2-D spectrum (*i.e.*, the image coming from the telescope) into a 1-D spectrum (a complex image processing task in and of itself), high-frequency noise in the spectrum is removed with a low-pass filter. A redshift estimate is obtained from the spectrum (*e.g.*, from SNID) and the spectrum is de-redshifted to its rest frame. The spectrum is re-binned to a consistent set of bins that are evenly spaced in log-space (*i.e.*,  $\log \lambda_i - \log \lambda_{i-1}$  is constant).

Next, the continuum (the blackbody component to the spectrum) is removed by fitting and dividing by an N-point spline fit on the spectrum, where N is commonly around 10 to 13. Blondin & Tonry (2007) notes that this removes all remaining color information from the spectrum. Continuum removal leads to artifacts at the edges of the spectrum, which can be smoothed by multiplying the edges by a cosine, a process known as apodizing. Finally, the spectrum is normalized (*e.g.*, to mean zero, or to between 0 and 1, or to however else is desired).

The preceding preprocessing is done by SNID and is detailed in Blondin & Tonry (2007).

### 3.2. Resampling spectra to low-resolution

The native resolution of each spectrum may vary, but when the spectra are re-binned by SNID they are all set to the common resolution of  $R = 738$ . This is considered high-resolution for SN classification, with bin-widths ranging from about  $6\text{\AA}$  to  $10\text{\AA}$  in the optical range. SNe are explosive processes and spectral features are broadened by the high velocity of the ejecta — typically 1,000s of  $\text{km s}^{-1}$ . We demonstrate (see Figure 4) that the performance of a classifier does not suffer when



the spectra it is trained on are re-binned to a much lower resolution. In fact, the classifier may even perform better if re-binning suppresses noise while preserving signal. This will enable the application of memory-intensive neural network architectures like the attention mechanism, which is  $O(N_{\text{wvl}}^2)$  for the number of wavelength bins in the spectrum,  $N$ . ABC-SN is trained on data that is lowered to  $R = 100$ .

While we could simply re-bin our spectra to reduce memory costs, it is more interesting to answer the question “What is the lowest resolution I need to collect my spectra at in order to responsibly use spectroscopic resources?” After processing the spectra following the SNID steps, we convolve them with a Gaussian that serves as a generic approximation of a spectrograph’s instrumental response in order to simulate a native low-resolution spectrum.

The Gaussian’s Full Width Half Maximum (FWHM) is defined as a function of bin-width. That is,

$$G(\mu_i, \sigma_i) = G(\lambda_i, \sigma(\Delta\lambda_i))$$

where  $G$  is a Gaussian function with mean  $\mu_i$  and standard deviation  $\sigma_i$ ,  $\lambda_i$  is the wavelength of the center of bin  $i$ , and  $\Delta\lambda_i$  is the size of bin  $i$ . We choose  $\text{FWHM} = \Delta\lambda_i R_{\text{original}}/R_{\text{lowered}}$ , and the standard deviation of a Gaussian is related to its FWHM by  $\text{FWHM} = 2\sigma\sqrt{2\ln 2}$ . We normalize  $G$  such that its integral along the spectrum is unity so that the convolution does not add or remove flux from the spectrum.

The last step in obtaining the low-resolution spectrum is to linearly interpolate the convolution (which is defined on the original spectrum’s wavelength bins) to the low-resolution wavelength bins. Figure 3 shows an example of a spectrum at the original  $R = 738$ , the resolution of the *SED*M  $R = 100$ , and the ultra-low-resolution  $R = 25$ .

With this new low-resolution version of our dataset, we show that DASH does not suffer any loss in classification power down to  $R \approx 25$ . Figure 4 shows the performance of DASH at the resolutions between  $R = 738$  and  $R = 25$ .

Further investigation of optimal resolution and signal-to-noise ratio for spectra collection will be the focus of a separate paper. In this work, we settle to perform our classification at a conservative  $R = 100$  resolution.

### 3.3. Culling, Standardizing and Validating

Each spectrum is defined from 2,500Å to 10,000Å, but we set each spectrum’s flux value to 0 at wavelengths shorter than 4,500Å and longer than 7,000Å to enforce uniformity. While this is a restricted wavelength range it served to ensure our data was maximally homogeneous

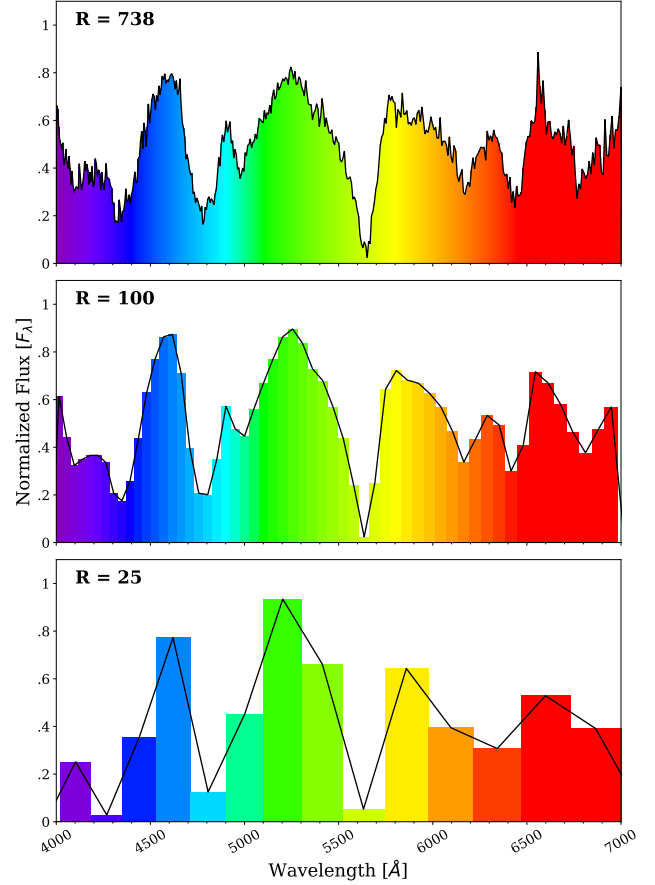


**Figure 3.** Three spectra from SN1998dt, a type Ib SN, observed 1.8 days after peak brightness. The blackbody continuum has been removed. Type Ib SNe do not show hydrogen spectral lines nor the SiIII line at 6355Å that characterizes SNe Ia. *Top:* The spectrum is plotted at the original high-resolution of  $R = 738$ . *Middle:* The spectrum is plotted at the low-resolution of  $R = 100$ , the same resolution that the *SED*M operates at. *Bottom:* The spectrum is plotted at the ultra-low-resolution of  $R = 25$ .

and avoid working with missing values. We also normalize each spectrum to be mean 0 and standard deviation 1, not including the 0-padding. At this point, we remove any spectra that have either a very small (0.1) or very large (100) dynamic range (the difference between a spectrum’s minimum value and maximum value).

Our spectral dataset exhibits extreme class imbalance, with our most numerous class, Ia-norm, making up over 56% of the dataset while the smallest class, Ibn represents less than 1%. Machine learning best practices dictate that it is important to stratify the train-test split — ensuring that if the training set represents  $X\%$  of the total dataset, then  $X\%$  of the occurrences of each class should be in the training set to avoid enforcing biases in the classifier (as discussed in Section 2).

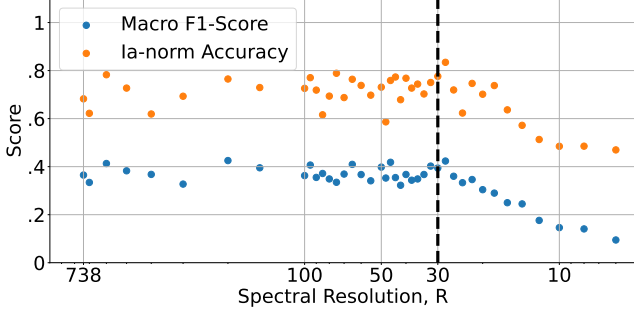


**Figure 4.** This figure shows how the performance of DASH changes as a function of the spectral resolution of the dataset it is trained on. We lower the spectral resolution of our dataset to 40 different values between the native resolution,  $R = 738$  and  $R = 5$  in order to examine how the performance of DASH would change. In blue, the macro F1-score on the test set is plotted at 41 different spectral resolutions. In orange, the model’s accuracy to predict SNe Ia-norm — the most numerous of the ten classes — is plotted. We qualitatively identify  $R \approx 30$  as the threshold below which DASH loses predictive power. Note that here DASH is trained with a decontaminated training-test split and early stopping to avoid overfitting (see Section 2).

Due to the small number of SNe in some classes, we did not split our data into a training-validation-test set. Thus, our model hyperparameters are selected based on test set performance.

### 3.4. Data Augmentation

We employ three data augmentation techniques on our training set. First, we add some white noise with mean  $\mu_{\text{noise}} = 0$  and a standard deviation  $\sigma_{\text{noise}} = 0.10$  to each spectrum. Next, we randomly shift the spectra by at most five bins red or blue (up to  $225\text{\AA}$  on the blue end and  $350\text{\AA}$  on the red end), simulating inaccurate redshift corrections. Finally, we loosely simulate telluric lines by injecting 0 to 4 spikes along the (standardized) spectra. These spikes are distributed uniformly across the non-zero part of each spectrum. The magnitude of each spike is drawn from a  $\mathcal{N} \sim (0, 2\sigma)$  where  $\sigma$  is the standard deviation of the spectrum itself. The sign of the spike — *i.e.*, whether it is in emission or absorption — has an 80% chance to be in emission (telluric lines are of course, in absorption, but we commonly find artifact spikes in correspondence with the location of telluric lines caused by their removal). The details of these augmentation techniques are collated in Table 3.

In order to balance the dataset, we generate many copies of each spectrum and perform the augmentation described above separately on each copy. Enough copies of the spectra from each class are generated such that all classes have roughly equal size (see the fourth column in Table 1). No oversampling or data augmentation is

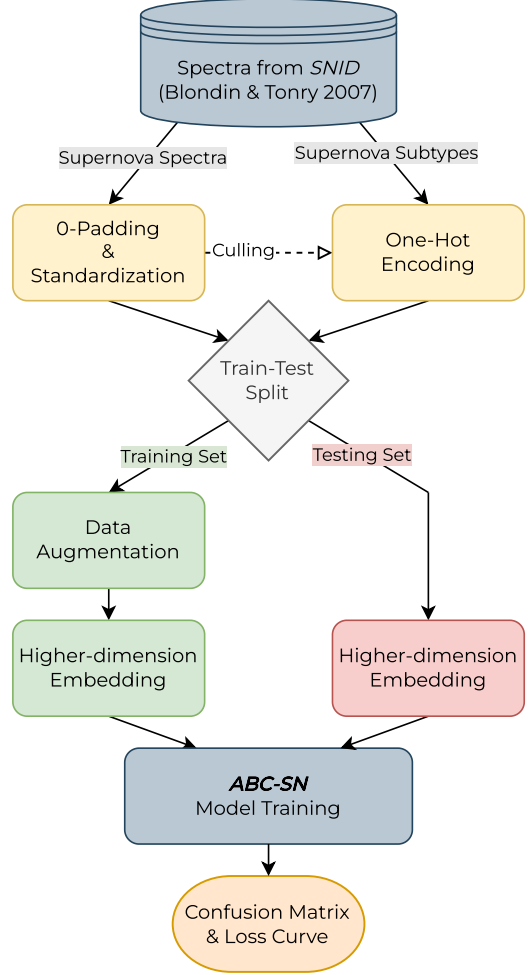


**Figure 5.** A flowchart that summarizes the operations we perform on our spectral data. All preprocessing steps are described in Section 3.1.

applied to the test set. Our workflow is summarized graphically in Figure 5.

## 4. METHODS AND MODELS

Here we describe the development of ABC-SN, including all architectural elements and evaluation metrics.

### 4.1. Model Performance Metrics

In the presence of an imbalanced dataset, appropriate performance metrics must be chosen to assess the performance of the model.

Precision, also known as ‘positive predictive value’, answers the question “How many retrieved items are relevant?” Recall, also known as ‘sensitivity’, answers the question “How many relevant items are retrieved?” While accuracy can be calculated for all classes at once, precision and recall must be calculated for each class separately.

$$\text{Precision} = \frac{TP}{TP + FP}$$

$$\text{Recall} = \frac{TP}{TP + FN}$$

$$F_1 = \frac{2TP}{2TP + FP + FN}$$

By calculating the F1-score for each class in a dataset and taking their *unweighted* average, we arrive at the ‘macro F1-score’. The macro F1-score provides a much more balanced picture of the model performance than, *e.g.*, accuracy, when dealing with an unbalanced dataset. It is for this reason that we consider the macro F1-score to be the most appropriate metric when comparing models for this analysis. It is the F1-score of the test set that we monitor during training.

#### 4.2. ABC-SN: An Attention-Based Classifier

The architecture of ABC-SN is broadly inspired by the Transformer (Vaswani et al. 2017). Modifications are needed to apply this model, natively built for Natural Language Processing (NLP), to spectral data. Here we describe how we adapted each element of the architecture inherited from the Transformer, including a discussion of choices that we ultimately abandoned, so as to aid researchers engaging in similar projects. ABC-SN is implemented in TensorFlow Keras (Chollet et al. 2015).

We must clarify immediately that we only include the encoder elements of the Transformer in our architecture since our purpose is inferential, rather than generative.

The architecture of ABC-SN, illustrated in Figure 6, begins with the input spectra, assumed to have shape  $(1, N_{wvl})$  where  $N_{wvl}$  is the number of wavelength bins that a spectrum is defined on. These spectra are then embedded into a higher dimension, described in Section 4.2.1. Next, positional information is encoded into the spectra (Section 4.2.2) before being passed to the encoder block (Section 4.2.3). Finally, data passes to the feed-forward classification head (Section 4.2.4), which provides the final output classification probabilities.

##### 4.2.1. The Embedding

From the observatory to our database, a spectrum is preprocessed into a 1-D vector (see Section 3.1). However, the attention mechanism was not designed with 1-D inputs in mind — the positional encoding is typically applied by concatenation, sum, or dot-product, so the first action in our model is to increase the dimensionality of a spectrum vector.

We tested five different embeddings to take our 1-dim spectra into a higher-dimensional space that would be more friendly to the Transformer architecture. The first

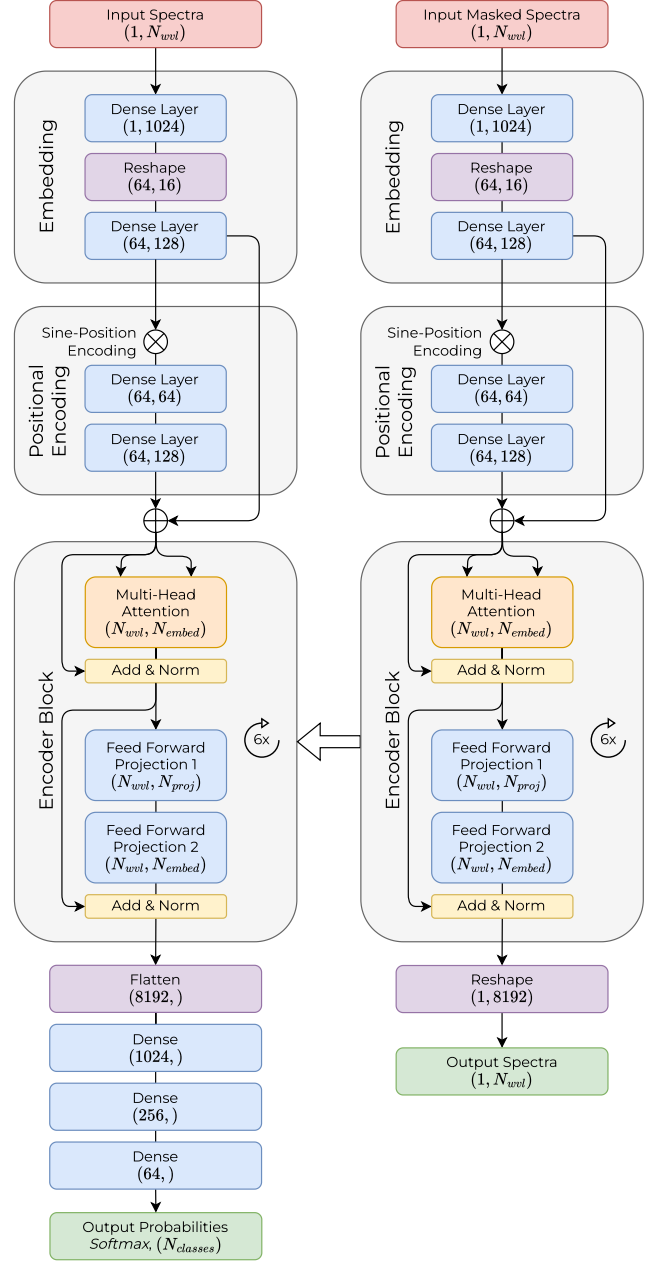


**Figure 6.** The conceptual diagram of the ABC-SN architecture described in Section 4.2.

was to bin each flux value in the spectra according to what quantile that flux value was in within the distribution of that spectrum. For example, suppose we decide to embed into  $N_{embed}$  dimensions. We would histogram the flux values of the spectrum into  $N_{embed}$  bins, and we would populate a  $(N_{wvl}, N_{embed})$  array with ones according to which bin each flux value falls into. This method proved not significantly better than having no embedding at all.



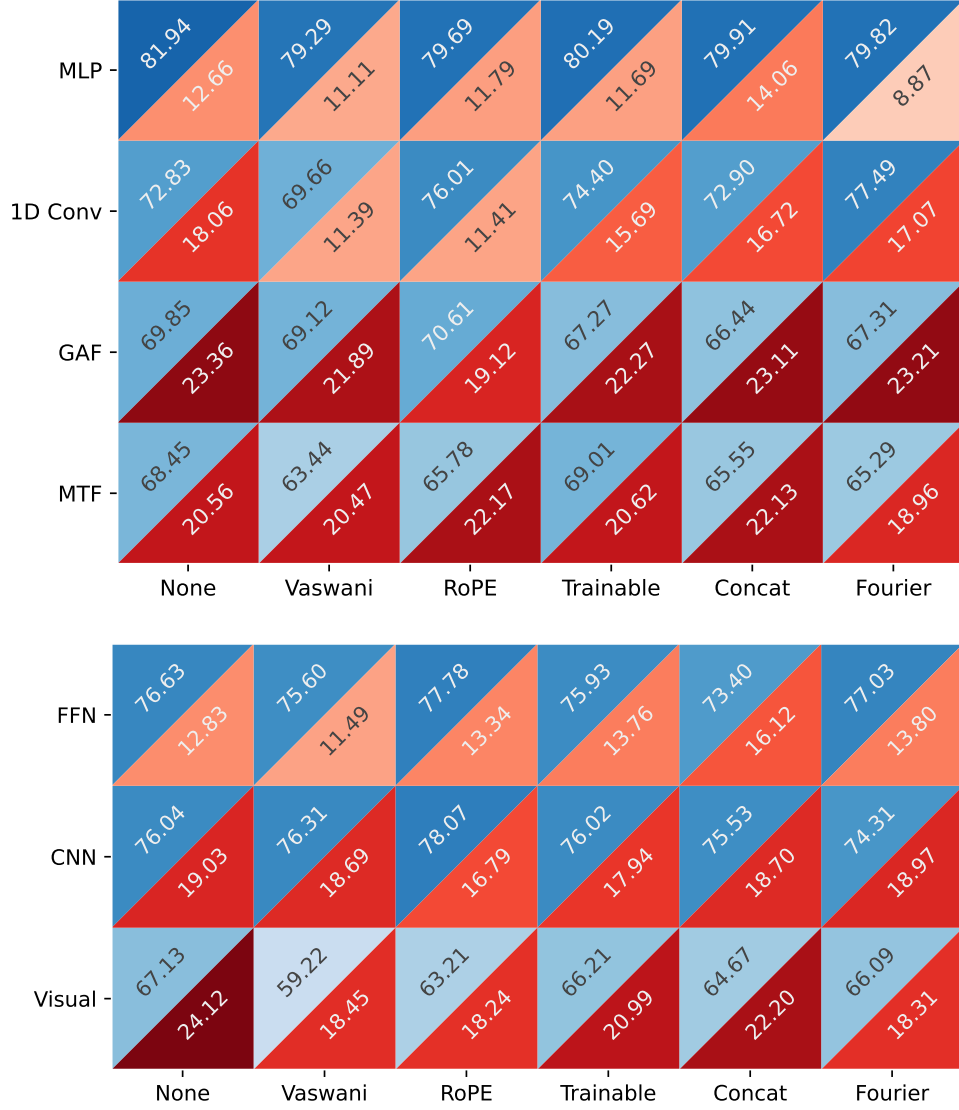


**Figure 7.** Results of tests performed on different architecture element combinations. *Top:* each box corresponds to a combination embedding ( $y$  axis) — positional encoding ( $x$  axis) as labeled and described in sections 4.2.1 and 4.2.2, respectively and average over the three tested options for classification heads (see Section 4.2.4). *Bottom:* each box corresponds to a combination classification head ( $y$  axis) — positional encoding ( $x$  axis) as labeled, average over the four embeddings. The top triangle in each cell corresponds to the test set F1-score, the bottom to the amount of overfitting, defined as the difference in F1-score between training and test sets. The selected architecture for ABC-SN corresponds to the top right cell of these plots: MLP embedding and Fourier positional encoding, Feed Forward (FF) classification head. While this combination does not achieve the highest F1-score it is at most two percentage points off from the best performer and shows the least amount of overfitting (colors: darker blues indicate higher F1-score, darker reds indicate more overfitting).

We then applied two methods from `pyts`, a Python package for time series classification (Faouzi & Janati 2020). The Gramian Angular Field (GAF) and Markov Transition Field (MTF) are images obtained from time series and we used a `pyts` implementation of a function to calculate a GAF and MAF from our 1-D spectra. We transformed each spectrum into a GAF or MAF before passing it to ABC-SN for training. However, we found that both the GAF and MAF generally performed worse than having no embedding.

The fourth embedding method is a learned embedding which uses a `Conv1D` layer with a kernel size of 1 and  $N_{\text{embed}}$  filters to project the 1-D spectra into an  $N_{\text{embed}}$ -dimensional space.

The fifth embedding method, the one that we adopted for ABC-SN, is also a learned embedding. Inspired by *Astroconformer* (Pan et al. 2024), we use a multi-layer perceptron (MLP) to embed the spectra into a higher dimension. The first layer of the MLP is a `Dense` layer with 1024 neurons and a linear activation function. This reshapes the spectra from  $(1, N_{\text{wvl}})$  to  $(1, 1024)$ . Next, we reshape the tensor to  $(64, 16)$  and pass this to another `Dense` layer with 128 neurons and a `ReLU` activation function, leading to a final data shape of  $(64, 128)$ . This tensor is passed to the positional encoding. This embedding is illustrated in Figure 6.

#### 4.2.2. The Positional Encoding

A key element of the Transformer architecture, and of ABC-SN, is the positional encoding (PE) which conveys the wavelength information for a given flux to the attention layers. A PE can be fixed or have learnable weights (Gehring et al. 2017; Ahmed et al. 2022). We looked to Moreno-Cartagena et al. (2023) and Pan et al. (2024) for their work on the attention mechanism applied to photometric light curves in order to find a PE to implement in ABC-SN. We tested six different PEs: No PE; “Vaswani” the PE used in Vaswani et al. (2017); “RoPE” or Rotary PE, used in Pan et al. (2024); “Fourier”, “Trainable”, “Concat” all described in Moreno-Cartagena et al. (2023). Based on a comparative test between all six methods, we decided on the “Fourier” PE for ABC-SN as it offers the best balance of performance and overfitting. The results of the comparative architecture test can be seen in Figure 7, marginalized over three classification heads (described in Section 4.2.4).

The Fourier PE is based on the PE used in Vaswani et al. (2017) but modulates that PE with a hidden `Dense` layer with a `GeLU` activation function. The output of this hidden layer is then supplied to another `Dense` layer with a linear activation function. We chose the hidden

layer to have 64 neurons, while the number of neurons in the output layer is chosen such that the output shape matches the input shape. The PE is then added to the spectral data just before being passed to the first `MultiHeadAttention` layer. This PE is illustrated in Figure 6.

#### 4.2.3. The Encoder Block

The encoder block is composed of two sub-blocks: the attention sub-block and the projection sub-block, explained graphically in Figure 6. The first sub-block includes the eponymous `MultiHeadAttention` (MHA) layer, which accepts two arguments to calculate attention on. Since we only use the encoder from the Transformer architecture, we are interested in self-attention, as per Vaswani et al. (2017), so we supply the layer with two copies of the inputs. The inputs to the MHA layer are directly added to its outputs, and this sum is normalized with a `LayerNormalization` layer. The summing of inputs and outputs out of sequence is called a ‘residual connection’. Note that this sub-block does not change the shape of the data passing through it.

The second sub-block projects the data from shape  $(N_{\text{wvl}}, N_{\text{embed}})$  to  $(N_{\text{wvl}}, N_{\text{proj}})$ . It should be the case that  $N_{\text{proj}} > N_{\text{embed}}$  based on the original reasoning for the projection layer outlined in Section 3.3 of Vaswani et al. (2017), though it is technically possible for it to be any positive integer. We implement this projection sub-block with a `Conv1D` layer with a kernel size of 1,  $N_{\text{proj}}$  filters and a `ReLU` activation function. The data is then projected back down from  $(N_{\text{wvl}}, N_{\text{proj}})$  to  $(N_{\text{wvl}}, N_{\text{embed}})$  with another `Conv1D` layer with a kernel size of 1,  $N_{\text{embed}}$  filters and a `ReLU` activation function. Just like the attention sub-block, we use a residual connection between the inputs and outputs of the projection sub-block and then normalize it with a `LayerNormalization` layer. Once again, this sub-block does not change the shape of the data passing through it.

The encoder block can be repeated as many times as desired, passing the outputs of one encoder block as the inputs of the next. Because the shape of the data going into the encoder block is preserved, there is no hard limit to the number of encoder blocks in a model. Providing each encoder block after the first with a residual connection of the PE by itself may help the model retain information about relationships between individual flux values. Encoder blocks may also be given a residual connection to the original spectral data or even to the output of one or more preceding encoder blocks.

We use a **Keras-NLP** implementation of the transformer encoder block, and we use a dropout value of 50%.

At this point in the architecture of the model, we hope that it has learned important information about how flux values in a spectrum relate to one another. Generally speaking, this is the information that a professional SN scientist would make a classification on and so the following neural network is designed for the same task.

#### 4.2.4. The Feed-forward Classification Head

The last element of the architecture of **ABC-SN** is the classification head. The data exiting the encoder block will be 2-D. To transform it to the final 10-neuron 1-D layer representing probabilities for each class, we use three **Dense** layers with  $N_{FF_1}$ ,  $N_{FF_2}$ , and  $N_{FF_3}$  neurons respectively, each with a **ReLU** activation function. Finally, the model concludes with a **Dense** layer with a Softmax activation function and ten neurons, one for each SN subtype in the dataset.

Each **Dense** layer is given an L2 regularization of 0.01, and each **Dense** layer is followed by a **Dropout** layer with a dropout of 50%.

Two alternatives for this classification head were trialed during **ABC-SN** development. The first was a CNN hybrid model. The output of the encoder was passed to several convolutional layers before being passed to the three-layer feed-forward network previously described. This constituted a significant increase in model complexity with an insignificant change in performance compared to the feed-forward only classification head.

The second alternative is an adaptation of the visual attention model presented in Yan et al. (2019), which was designed for automated melanoma recognition. Their model uses **VGG-16** (Simonyan & Zisserman 2015), a widely used convolutional network, as a backbone and then incorporates attention layers. For our trials, this visual attention model also replaces the encoder portion of **ABC-SN** and is overall more complex, though still relying on **Conv2D** and **MultiHeadAttention** layers. This architecture did not improve the performance.

The results of the comparative trials between these basic model architectures is reported in Figure 7.

#### 4.3. Pretraining Attention Weights on Masked Spectra

One of the major steps we took to combat overfitting was to train the model in two stages. Inspired by masked language models (Devlin et al. 2019), the first stage ‘pre-trains’ the weights of the encoder block on the regression task of predicting masked spectral values, while the second stage trains **ABC-SN** with the weights in the encoder layers initialized from the pretraining.

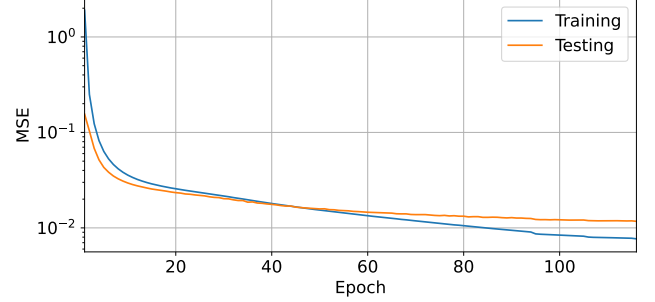


**Figure 8.** The loss curve during **ABC-SN** pretraining. The mean squared error (MSE) is shown for the training and test sets during pretraining. The model was pretrained for 141 epochs on reconstruction of masked spectra (see subsection 4.3) before reverting back to epoch 116 due to an early stopping callback.

We do this by constructing an **ABC-SN** model that is truncated after the encoder blocks, shown on the right in Figure 6. The output of the encoder blocks is flattened and then connected to the output layer, which is a **Dense** layer with a linear activation function and the layer bias turned off. The inputs *and* targets for this pretraining model are SN spectra, so the number of neurons in the final **Dense** layer is equal to the size of the inputs.

The target spectra for the pretraining model are untouched, but the input spectra are masked and perturbed. A random, continuous 15% of the non-zero portion of each spectrum is selected and set to 0. An additional 2.5% of points on the non-zero portion of each spectrum is randomly perturbed by multiplying it with a Gaussian random variable with mean 0 and standard deviation 1. The weights of this model are trained to predict masked spectra values in order to generate a rich internal representation of the data.

The loss function for this pretraining stage is shown in Figure 8. At the end of pretraining, the weights for all of the encoder sub-layers are used to initialize the weights for those layers in the full **ABC-SN** model.

#### 4.4. Computation Costs

**ABC-SN** was trained on one Nvidia T4 GPU for 15 minutes. The pretraining model was trained on the same GPU for 10 minutes. With the same hardware, **ABC-SN** takes  $242 \pm 4.19$  ms to predict on the test set (1880 spectra,  $128 \mu s$  per spectrum).

We retrained **DASH** with 16 CPUs and 64GB RAM. When retraining **DASH** with the original training schema (see Figure 1, left), training lasted 36 hours (576 CPU hours). When the early stopping protocols are enabled, **DASH** training lasted 45 minutes (12 CPU hours; see Figure 1, right). With the same hardware, **DASH** retrained

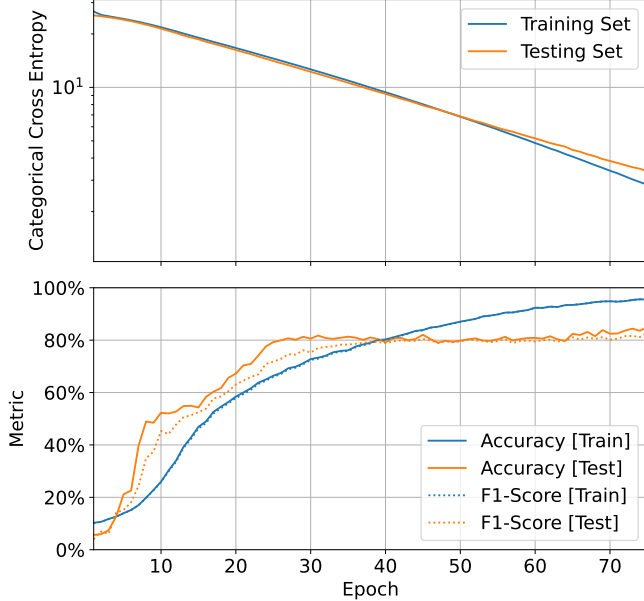


**Figure 9.** The loss and metric curves for ABC-SN during training. *Top:* The categorical cross-entropy loss. *Bottom:* The categorical accuracy (solid lines) and macro F1-score (dotted lines). ABC-SN was set to train for 100 epochs before reverting back to epoch 75 due to an early stopping callback. The rapid rise of the training set metrics beyond the test set demonstrates this data’s eagerness to overfit despite our significant efforts in regularization to prevent this.

SN Subtype	Completeness		Purity	
	ABC-SN	DASH	ABC-SN	DASH
Ia-norm	87.6%	61.6%	94.9%	92.5%
Ia-91T	83.2%	76.2%	64.7%	23.5%
Ia-91bg	82.4%	50.4%	76.1%	66.0%
Iax	100%	94.1%	85.0%	58.5%
Ib-norm	73.2%	60.5%	81.2%	61.9%
Ibn	100%	25.0%	85.7%	100%
Iib	75.3%	44.8%	75.3%	59.1%
Ic-norm	87.2%	59.1%	58.2%	25.7%
Ic-broad	73.9%	51.9%	97.6%	51.9%
IIP	95.7%	95.3%	97.8%	67.2%

**Table 2.** Per subtype accuracy of ABC-SN compared to DASH, retrained in this dataset with updated training-test split and preventing overfitting. The first two columns show per-class prediction completeness, the last two purity.

to avoid overfitting takes  $8.07 \text{ s} \pm 79.8 \text{ ms}$  to predict on the test set (143,920 spectra,  $56 \mu\text{s}$  per spectrum).

## 5. RESULTS AND DISCUSSION

To ensure ABC-SN’s performance would extend to newly discovered SNe we evaluate overfitting by mon-

itoring the model loss at every training epoch on both training and test sets. Figure 8 shows the mean squared error (MSE) loss during ABC-SN pretraining (masked model predictions, see Section 4.3). Figure 9 shows the categorical cross-entropy loss during ABC-SN training (classifier model). During both training and pretraining, we use an early stopping callback to prevent overfitting and avoid wasting computation resources (see details in Appendix, Table A). ABC-SN trained for a total of 100 epochs when the early stopping callback was activated; the final model represents 75 trained epochs.

The final accuracies on the training and test sets are 85.05% and 98.33%. The final macro F1-scores are 83.01% and 98.31%. DASH accuracies on the training and test sets are 61.97% and 67.84%; DASH macro F1-scores are 58.86% and 77.06%.

A confusion matrix showing per-class performance is shown in Figure 10 (and additional confusion matrices showing precision/purity and recall/completeness are included in Appendix B). Table 2 shows the performance for each subtype for both ABC-SN and the DASH benchmark model.

For nearly all classes, ABC-SN outperforms DASH. Notably, it outperforms DASH by 26% points on SN Ia completeness and 2.4% in SN Ia purity. The only exception is purity on the SN Ibn sample, but the small size of the sample (27 viable spectra of 3 SNe, only 1% of the test set — see Table 1 and Figure 2) makes estimates of the performance on this subclass unreliable.

Since we did not train our model with the goal of maximizing the purity of a SN Ia sample, as one would do for a classifier primarily aimed for use in cosmology, we cannot directly compare the performance of ABC-SN to SNIAscore. However, we note that from Figure 4 of Fremling et al. (2021) at a purity comparable to that of ABC-SN (5%) their model accuracy appears to be 92% compared to our 88%. Nonetheless, our model can classify 10 subtypes of SNe and is therefore of broader applicability than SNIAscore.

## 6. CONCLUSION AND FUTURE WORK

We developed a new, attention based model for the automated classification of supernovae (SNe) spectra into 10 subtypes, including subtypes of thermonuclear, core collapse and stripped envelope supernovae, and we compared its performance with the popular neural network based classifier DASH (Muthukrishna et al. 2019).

Our model does require the spectra to be preprocessed through the SNID preprocessing steps, including continuum removal, telluric line removal, de-redshifting, zero-padding, and additionally ABC-SN needs to be served spectra at resolution  $R = 100$ . Alternatively, modifi-

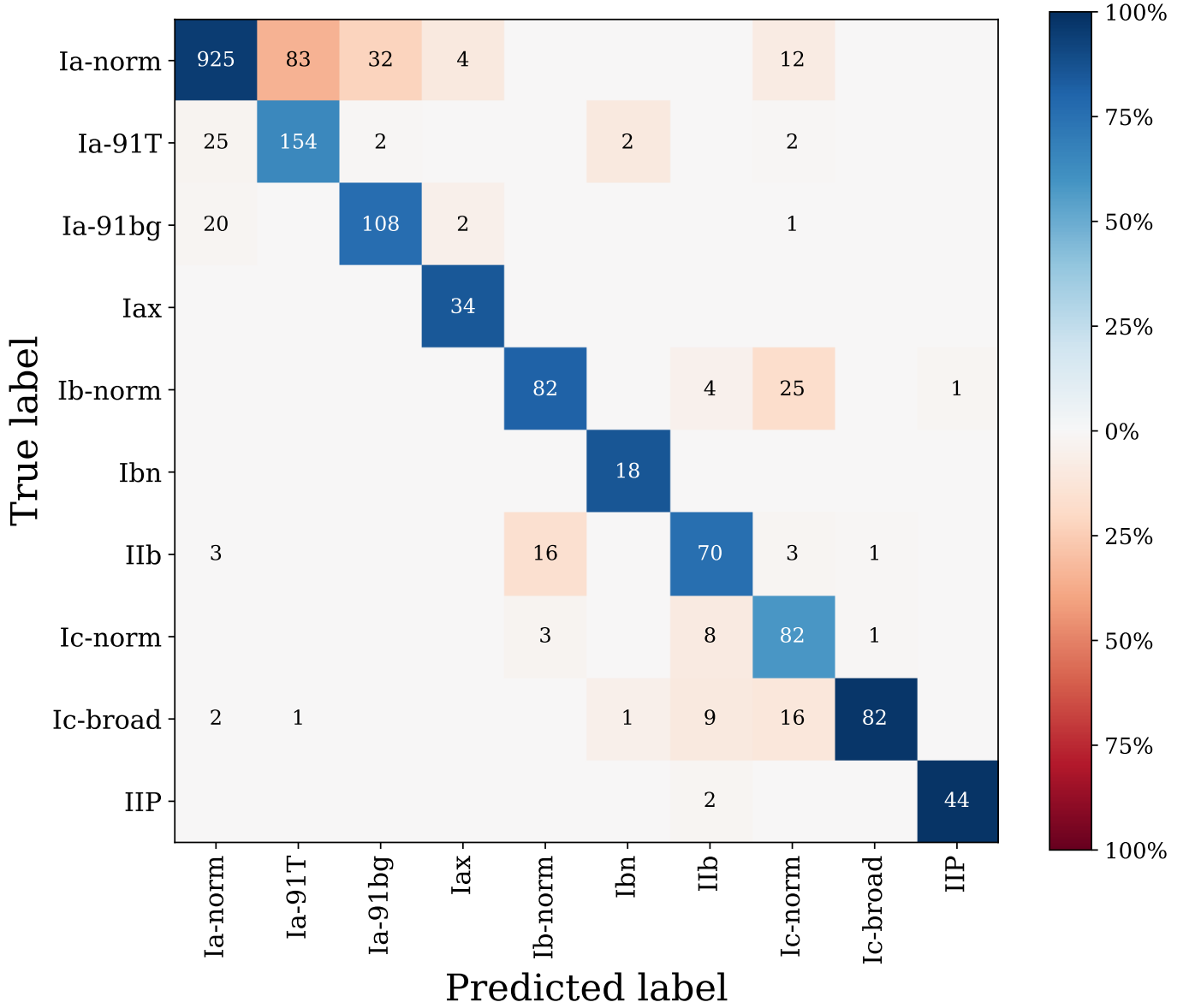


**Figure 10.** Confusion matrix showing the performance of ABC-SN in the classification of SNe in the SNID dataset. On the horizontal axis, the predicted class. On the vertical axis, the label. As in figure Figure 1, cells on the diagonal (correct classifications) are plotted in shades of blue and off-diagonal (incorrect) in shades of red corresponding to the percentage (in)accuracy. The percentage is calculated along the columns (emphasizing completeness). In each cell, the number of objects with the corresponding prediction and label is reported, when that number is larger than 0 (note the significance class imbalance in the test set, discussed in section 3). This confusion matrix shows the clear and significant improvement over the state of the art, DASH (see Figure 1, right top panel) on the classification of 10 selected subtypes. The model performance is discussed in detail in section 5. A set of confusion matrices normalized by column (emphasizing completeness) and by row (emphasizing purity) are available in B with percentage performance reported in each cell.



cations of the input layer shape and fine tuning would enable other resolutions. This is a potential limitation of its applicability, especially if spectra at high redshift are to be classified, as key features may shift inside the padding region. However, this setup allowed us to directly test and compare different architectures on a homogeneous dataset. Conversely, some relatively small future upgrades to our architecture may include embedding wavelength and flux together before applying positional encoding. While this is not currently necessary since our spectra are evenly sampled, this may improve classification in a broader range of redshifts.

Our model was trained on a dataset of 3,764 spectra from 498 SNe, mostly composed of SNID template spectra. We lower the resolution of each spectrum from  $R = 738$  to  $R = 100$  to enable the development and use of an attention-based neural network, which is memory-intensive. In Section 3.2 and Figure 4 we demonstrate that lowering the resolution of spectral data does not negatively impact model performance.

To enable a direct and fair comparison and to establish our domain benchmark, we retrained DASH to address two issues: overfitting and the contamination of spectra from the same SN in both training and test data (see Section 2). We introduced an early stopping callback to prevent overfitting and rigorously enforced that all spectra from the same SN are only in the training or in the test set.

Special attention is given to the training of ABC-SN, including ensuring that in train-test split all spectra from a given SN are placed in either the training or the test sets and applying data augmentation to the training set in order to balance the dataset and reduce model bias towards the most numerous classes (see Section 3).

We explored a variety of architectural choices (described in detail in Section 4.2) and we made our final choice with the goal of delivering a model that reaches high performance with limited overfitting to ensure transferability. Our final model is inspired by the Transformer (Vaswani et al. 2017). It includes a trainable positional encoding (Section 4.2.2), the multi-head attention mechanism as well as a generative, pretraining stage on masked spectra (see Section 4.3).

ABC-SN improves upon DASH as a spectroscopic new-SN classifier, providing higher classification accuracy for 10 SN classes. We measure the performance of DASH with the macro F1-score, which accounts for dataset imbalance. ABC-SN attains a macro F1-score of 83.01% while DASH’s macro F1-score retrained on the same dataset reaches 58.86%. A detailed performance assessment is provided in Section 5 and visualized in Figure 10 and Appendix B. The model recall exceeds 75% on all

classes, the model precision falls below 75% only for SN Ia-91T and SN Ic. SN Ia-91T are contaminated by closely related subtypes of SN Ia (91T, 91bg, and Iax) and of SN Ic by stripped envelope SNe Ib.

While our model is not optimized for cosmology, the purity of the SN Type Ia-norm classification is 95%. Since we are releasing this as an open-source software package, the user could easily retrain the model to maximize Ia-norm purity.

SNID is still the ubiquitous method for spectroscopic SN classification, and in fact we used SNID labels as our ground truth in training. However, AI-based methods offer greater automation options and require limited computational resources once trained, making them well-suited to the era of data-intensive astronomy.

With the development of ABC-SN, we have identified a potential performance ceiling for neural network SN classifiers. After testing thousands of different models, we suspect a higher performance may not be achieved on this dataset with improved architectural choices due to label noise (*i.e.*, mislabeled spectra), especially for the rarer SN subtypes, as well as classification schema based on an assumed rigid taxonomy. Any SN is driven by continuous variables like progenitor mass, progenitor metallicity, circumstellar material composition, etc., and yet we perform classification of SNe into discrete subtypes. Although there do exist some known discrete categories of SNe (*e.g.*, thermonuclear vs. core collapse), the practice of classifying SNe into rigid subtypes is questionable. Alternative approaches (*e.g.*, Williamson et al. 2019; Kou et al. 2020; S. de Souza et al. 2023) and hierarchical classification schemes (Villar et al. 2023; Shah et al. 2025), are being developed and may well result in more meaningful solutions. Nonetheless, classification remains an important and widespread practice as it enables the planning of follow-up resources and the construction of samples that support studies into different SN physical processes. Furthermore, neural network-based classifiers naturally provide a probabilistic classification, which allows users to redefine spectral labels.

We further acknowledge that SNID and DASH provide not only class labels but also redshift and phase estimates. In this work, we only focus on SN subtype classification in order to provide an extensive exploration of neural network solutions and an effective tool for the community at the incipit of the *LSST* era. We expect the most common application of ABC-SN will be to classify newly discovered SNe, and we leave it to future work to extend ABC-SN to those additional tasks. ABC-SN could also be retrained on a larger dataset that includes non-SN transients; we leave this task as future work as well.

This work also demonstrates that SN classification with low-resolution spectra is perfectly viable. This is an important result since in the era of *LSST* when spectroscopic resources are extremely limited compared to the wealth of transient discoveries. In separate work, we will provide guidelines on the spectral resolution and signal-to-noise-ratio (SNR) necessary for different transient classification tasks. For the moment, ABC-SN is designed to classify spectra at the resolution of the *SED-Machine* (Blagorodnova et al. 2018),  $R = 100$ , and we provide methods to lower higher resolution spectra to  $R = 100$  for the application of ABC-SN.

ABC-SN is an open source tool<sup>2</sup>, we provide a pre-trained model ready for application, together with tools for preprocessing spectra, and we provide the code base

and hope the astrophysical community will continue to refine ABC-SN for additional applications.

WFF and FBB acknowledge support from the National Science Foundation Award No. AST-2108841.

The authors acknowledge the support of the Vera C. Rubin Legacy Survey of Space and Time Science Collaborations and particularly of the Transient and Variable Star Science Collaboration (TVS SC), which provided opportunities for collaboration and exchange of ideas and knowledge.

Special thanks are also given to the penguins, polar bears, and all else who live in cold climes. Polar habitats are degraded by heat generated from our computing tasks; we hope their unwilling sacrifice will not be in vain.

## APPENDIX

### A. ABC-SN TRAINING HYPERPARAMETERS AND DATA PREPARATION CHOICES

ABC-SN training hyperparameters and data preparation choices are reported in Table 3.

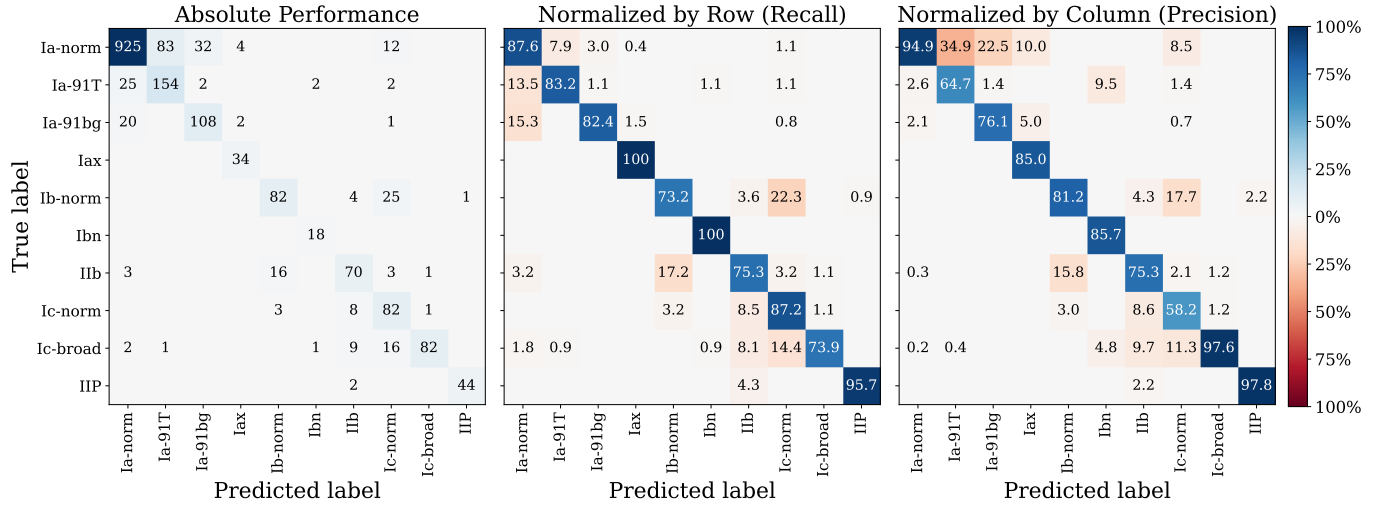
### B. COMPLETE PERFORMANCE ASSESSMENT OF ABC-SN

Figure 11 shows a holistic view of ABC-SN performance with three test set confusion matrices. The first shows the absolute performance of ABC-SN, providing raw values for the number of classified spectra. The second confusion matrix shows the same data but normalized by the number of true labels for each class. The percentages along the diagonal represent the completeness of ABC-SN for each class, answering the question, “What fraction of Class X was correctly classified?” The third confusion matrix shows the same data again but normalized by the number of predicted labels for each class. The percentages along the diagonal represent the purity of ABC-SN predictions, answering the question, “What fraction of spectra labeled as Class X were indeed Class X?”

<sup>2</sup> we will add a GitHub link here and also as astro software library link

<b>Preprocessing</b>		
Full wavelength range	2500 Å – 10,000 Å	Wavelength range of the input data.
Non-zero wavelength range	4500 Å – 7000 Å	Flux is padded to zero outside of this range.
Supernova phase range	[−20, 50]	Days since estimated to <i>V</i> band maximum.
Peak-to-peak range	[0.1, 100]	Spectra with a larger range are removed from the dataset.
Training set fraction	50%	
<b>Data Augmentation</b>		
Injected noise	$\sim \mathcal{N}(0, 0.01)$	Noise distribution.
Spectrum shifting	$N_{\text{shift}} \in [-5, 5]$	Shift spectrum by $N_{\text{shift}}$ wavelength bins drawn from a uniform (integer) distribution in this range.
Number of injected spikes	$N_{\text{spikes}} \in [0, 4]$	$N_{\text{spikes}}$ drawn from a uniform (integer) distribution in this range.
Injected spike sign	$p(+) = 0.8$	Probability of spike being in emission (+), otherwise absorption.
Spike amplitude	$2\sigma_i$	Where $\sigma_i$ is the standard deviation of the spectrum being augmented.
<b>Pretraining</b>		
Masking fraction	15%	Amount of each spectrum to mask for pretraining.
Mask value	0	Set the masked values to this value for pretraining
Batch size	64	Batch size of the pretraining network.
<i>Early stopping</i>		
Minimum improvement	$\Delta L = 0.0005$	Minimum improvement threshold in test MSE for early stopping.
Patience	$P_e = 25$	Training halted after $P_e$ epochs with test MSE improvement $< \Delta L$ .
Initial learning rate ( $lr$ )	$lr_{\text{start}} = 10^{-4}$	
<i>Reduce Learning Rate on Plateau (RLRP)</i>		
Minimum improvement	$\Delta L_{\text{RLRP}} = 0.0005$	Minimum improvement in test MSE for $lr$ updates.
Patience	$P_{\text{RLRP}} = 10$	$lr$ reduced after $P_{\text{RLRP}}$ epochs with improvement $< \Delta L_{\text{RLRP}}$ .
Factor	0.5	Reduce $lr$ by this factor.
Minimum $lr$	$lr_{\text{min}} = 10^{-7}$	RLRP will not reduce $lr$ below this threshold.
<b>ABC-SN Training</b>		
Batch size	64	Batch size of ABC-SN during training.
<i>Early stopping</i>		
Minimum improvement	$\Delta F1 = 0.005$	Minimum improvement threshold in test F1.
Patience	$P_e = 25$	Training halted after $P_e$ epochs with test F1 improvement $< \Delta F1$ .
Initial learning rate ( $lr$ )	$lr_{\text{start}} = 10^{-5}$	
<i>Reduce Learning Rate on Plateau (RLRP)</i>		
Minimum improvement	$\Delta L_{\text{RLRP}} = 0.0005$	Minimum improvement in test F1 for $lr$ updates.
Patience	$P_{\text{RLRP}} = 10$	$lr$ reduced after $P_{\text{RLRP}}$ epochs with improvement $< \Delta L_{\text{RLRP}}$ .
Factor	0.5	Reduce $lr$ rate by this factor.
Minimum $lr$	$lr_{\text{min}} = 10^{-7}$	RLRP will not reduce $lr$ below this threshold.

**Table 3.** A table of hyperparameter choices for ABC-SN. *Preprocessing* describes choices in data cleaning and culling (Section 3.1). *Data Augmentation* describes how we duplicated and modified spectra in order to balance our dataset and combat overfitting (Section 3.4). *Pretraining* hyperparameters account for the training scheme we used for the masked spectra regression model (Section 4.3). *ABC-SN Training* hyperparameters detail the training scheme for the predictive model (Section 4.2).



**Figure 11.** Confusion matrix for the release version of ABC-SN. In the first matrix, the data is not normalized and the numbers and colors reflect the absolute number of SN in each bin. The second matrix is normalized by row (*i.e.*, recall/completeness). The third matrix is normalized by column (*i.e.*, precision/purity).

## REFERENCES

- Ahmed, S., Nielsen, I. E., Tripathi, A., et al. 2022, Transformers in Time-series Analysis: A Tutorial, arXiv, doi: [10.48550/arXiv.2205.01138](https://doi.org/10.48550/arXiv.2205.01138)
- Andrew Howell, D., Sullivan, M., Nugent, P. E., et al. 2006, Nature, 443, 308
- Blagorodnova, N., Neill, J. D., Walters, R., et al. 2018, Publications of the Astronomical Society of the Pacific, 130, 035003, doi: [10.1088/1538-3873/aaa53f](https://doi.org/10.1088/1538-3873/aaa53f)
- Blondin, S., & Tonry, J. L. 2007, The Astrophysical Journal, 666, 1024, doi: [10.1086/520494](https://doi.org/10.1086/520494)
- Blondin, S., Matheson, T., Kirshner, R. P., et al. 2012, The Astronomical Journal, 143, 126, doi: [10.1088/0004-6256/143/5/126](https://doi.org/10.1088/0004-6256/143/5/126)
- Boone, K. 2019, AJ, 158, 257, doi: [10.3847/1538-3881/ab5182](https://doi.org/10.3847/1538-3881/ab5182)
- Cai, Y., Lin, J., Lin, Z., et al. 2022, in Proceedings of the IEEE/CVF Conference on Computer Vision and Pattern Recognition, 745–755
- Chollet, F., et al. 2015, Keras, <https://keras.io>
- Couch, S. M. 2017, Philosophical Transactions of the Royal Society A: Mathematical, Physical and Engineering Sciences, 375, 20160271, doi: [10.1098/rsta.2016.0271](https://doi.org/10.1098/rsta.2016.0271)
- Devlin, J., Chang, M.-W., Lee, K., & Toutanova, K. 2019, BERT: Pre-training of Deep Bidirectional Transformers for Language Understanding, arXiv, doi: [10.48550/arXiv.1810.04805](https://doi.org/10.48550/arXiv.1810.04805)
- Dosovitskiy, A., Beyer, L., Kolesnikov, A., et al. 2020, arXiv preprint arXiv:2010.11929
- Faouzi, J., & Janati, H. 2020, Journal of Machine Learning Research, 21, 1. <http://jmlr.org/papers/v21/19-763.html>
- Filippenko, A. V. 1997, Annual Review of Astronomy and Astrophysics, 35, 309, doi: [10.1146/annurev.astro.35.1.309](https://doi.org/10.1146/annurev.astro.35.1.309)
- Fremling, C., Hall, X. J., Coughlin, M. W., et al. 2021, The Astrophysical Journal, 917, L2, doi: [10.3847/2041-8213/ac116f](https://doi.org/10.3847/2041-8213/ac116f)
- Gal-Yam, A. 2017, in Handbook of Supernovae, ed. A. W. Alsabti & P. Murdin, 195, doi: [10.1007/978-3-319-21846-5\\_35](https://doi.org/10.1007/978-3-319-21846-5_35)
- Gehring, J., Auli, M., Grangier, D., Yarats, D., & Dauphin, Y. N. 2017, Convolutional Sequence to Sequence Learning, arXiv, doi: [10.48550/arXiv.1705.03122](https://doi.org/10.48550/arXiv.1705.03122)
- He, X., Chen, Y., & Lin, Z. 2021, Remote Sensing, 13, 498
- Hicken, M., Garnavich, P., Prieto, J., et al. 2007, The Astrophysical Journal, 669, L17
- Janka, H.-T., Hanke, F., Hudepohl, L., et al. 2012, Progress of Theoretical and Experimental Physics, 2012, 01A309
- Kasen, D., Woosley, S., & Heger, A. 2011, The Astrophysical Journal, 734, 102
- Khakpash, S., Bianco, F. B., Modjaz, M., et al. 2024, The Astrophysical Journal Supplement Series, 275, 37
- Koblischke, N., & Bovy, J. 2024, SpectraFM: Tuning into Stellar Foundation Models, arXiv, doi: [10.48550/arXiv.2411.04750](https://doi.org/10.48550/arXiv.2411.04750)
- Kou, S., Chen, X., & Liu, X. 2020, ApJ, 890, 177, doi: [10.3847/1538-4357/ab6601](https://doi.org/10.3847/1538-4357/ab6601)

- Kou, S., Chen, X., & Liu, X. 2020, *The Astrophysical Journal*, 890, 177
- Kunkel, W., Madore, B., Shelton, I., et al. 1987, *International Astronomical Union Circular*, 4316, 1. <https://ui.adsabs.harvard.edu/abs/1987IAUC.4316....1K>
- Liu, Y., & Modjaz, M. 2015, SuperNova IDentification spectral templates of 70 stripped-envelope core-collapse supernovae, arXiv, doi: [10.48550/arXiv.1405.1437](https://doi.org/10.48550/arXiv.1405.1437)
- Liu, Y.-Q., Modjaz, M., Bianco, F. B., & Graur, O. 2016, *The Astrophysical Journal*, 827, 90, doi: [10.3847/0004-637X/827/2/90](https://doi.org/10.3847/0004-637X/827/2/90)
- Matheson, T., Kirshner, R. P., Challis, P., et al. 2008, *The Astronomical Journal*, 135, 1598, doi: [10.1088/0004-6256/135/4/1598](https://doi.org/10.1088/0004-6256/135/4/1598)
- Mazzali, P. A., Röpke, F. K., Benetti, S., & Hillebrandt, W. 2007, *Science*, 315, 825, doi: [10.1126/science.1136259](https://doi.org/10.1126/science.1136259)
- Minkowski, R. 1941, *Publications of the Astronomical Society of the Pacific*, 53, 224, doi: [10.1086/125315](https://doi.org/10.1086/125315)
- Modjaz, M., Gutiérrez, C. P., & Arcavi, I. 2019, *Nature Astronomy*, 3, 717, doi: [10.1038/s41550-019-0856-2](https://doi.org/10.1038/s41550-019-0856-2)
- Modjaz, M., Liu, Y. Q., Bianco, F. B., & Graur, O. 2016, *The Astrophysical Journal*, 832, 108, doi: [10.3847/0004-637X/832/2/108](https://doi.org/10.3847/0004-637X/832/2/108)
- Modjaz, M., Blondin, S., Kirshner, R. P., et al. 2014, *The Astronomical Journal*, 147, 99, doi: [10.1088/0004-6256/147/5/99](https://doi.org/10.1088/0004-6256/147/5/99)
- Möller, A., & de Boissière, T. 2020, *MNRAS*, 491, 4277, doi: [10.1093/mnras/stz3312](https://doi.org/10.1093/mnras/stz3312)
- Moreno-Cartagena, D., Cabrera-Vives, G., Protopapas, P., et al. 2023, Positional Encodings for Light Curve Transformers: Playing with Positions and Attention, arXiv, doi: [10.48550/arXiv.2308.06404](https://doi.org/10.48550/arXiv.2308.06404)
- Moriya, T. J., Sorokina, E. I., & Chevalier, R. A. 2018, *Space Science Reviews*, 214, 59
- Muthukrishna, D., Parkinson, D., & Tucker, B. E. 2019, *The Astrophysical Journal*, 885, 85, doi: [10.3847/1538-4357/ab48f4](https://doi.org/10.3847/1538-4357/ab48f4)
- Pan, J.-S., Ting, Y.-S., & Yu, J. 2024, *Monthly Notices of the Royal Astronomical Society*, 528, 5890, doi: [10.1093/mnras/stae068](https://doi.org/10.1093/mnras/stae068)
- Perlmutter, S., Aldering, G., Goldhaber, G., et al. 1999, *The Astrophysical Journal*, 517, 565, doi: [10.1086/307221](https://doi.org/10.1086/307221)
- Qu, H., Sako, M., Möller, A., & Doux, C. 2021, *AJ*, 162, 67, doi: [10.3847/1538-3881/ac0824](https://doi.org/10.3847/1538-3881/ac0824)
- Riess, A. G., Filippenko, A. V., Challis, P., et al. 1998, *The Astronomical Journal*, 116, 1009, doi: [10.1086/300499](https://doi.org/10.1086/300499)
- Röpke, F. 2007, *Thermonuclear Supernovae*, Tech. rep.
- S. de Souza, R., Thorp, S., Galbany, L., et al. 2023, *Astronomy and Computing*, 44, 100715, doi: [10.1016/j.ascom.2023.100715](https://doi.org/10.1016/j.ascom.2023.100715)
- Sasdelli, M., Ishida, E. E. O., Vilalta, R., et al. 2016, *MNRAS*, 461, 2044, doi: [10.1093/mnras/stw1228](https://doi.org/10.1093/mnras/stw1228)
- Shah, V. G., Gagliano, A., Malanchev, K., Narayan, G., & The LSST Dark Energy Science Collaboration. 2025, arXiv e-prints, arXiv:2501.01496, doi: [10.48550/arXiv.2501.01496](https://doi.org/10.48550/arXiv.2501.01496)
- Silverman, J. M., Foley, R. J., Filippenko, A. V., et al. 2012, *Monthly Notices of the Royal Astronomical Society*, 425, 1789, doi: [10.1111/j.1365-2966.2012.21270.x](https://doi.org/10.1111/j.1365-2966.2012.21270.x)
- Simonyan, K., & Zisserman, A. 2015, Very Deep Convolutional Networks for Large-Scale Image Recognition, arXiv, doi: [10.48550/arXiv.1409.1556](https://doi.org/10.48550/arXiv.1409.1556)
- Vaswani, A., Shazeer, N., Parmar, N., et al. 2017, Attention Is All You Need, arXiv, doi: [10.48550/arXiv.1706.03762](https://doi.org/10.48550/arXiv.1706.03762)
- Villar, V. A., de Soto, K., & Gagliano, A. 2023, arXiv preprint arXiv:2312.02266
- Williamson, M., Modjaz, M., & Bianco, F. B. 2019, *The Astrophysical Journal Letters*, 880, L22
- Woosley, S. 2017, *The Astrophysical Journal*, 836, 244
- Woosley, S., & Janka, T. 2005, *Nature Physics*, 1, 147
- Woosley, S., & Kasen, D. 2011, *The Astrophysical Journal*, 734, 38
- Woosley, S. E., & Weaver, T. A. 1986, IN: *Annual review of astronomy and astrophysics*. Volume 24 (A87-26730 10-90). Palo Alto, CA, Annual Reviews, Inc., 1986, p. 205-253., 24, 205
- Yan, Y., Kawahara, J., & Hamarneh, G. 2019, in *Information Processing in Medical Imaging*, ed. A. C. S. Chung, J. C. Gee, P. A. Yushkevich, & S. Bao (Cham: Springer International Publishing), 793–804, doi: [10.1007/978-3-030-20351-1\\_62](https://doi.org/10.1007/978-3-030-20351-1_62)
- Yaron, O., & Gal-Yam, A. 2012, *Publications of the Astronomical Society of the Pacific*, 124, 668, doi: [10.1086/666656](https://doi.org/10.1086/666656)
- Zhang, G., Helfer, T., Gagliano, A. T., Mishra-Sharma, S., & Ashley Villar, V. 2024, *Machine Learning: Science and Technology*, 5, 045069, doi: [10.1088/2632-2153/ad990d](https://doi.org/10.1088/2632-2153/ad990d)
- Zhou, H., Zhang, S., Peng, J., et al. 2021, Informer: Beyond efficient transformer for long sequence time-series forecasting